Kinetic study of gold nanoparticles synthesized in the presence of chitosan and citric acid

Silviya Simeonova[a,*], Peter Georgiev[a], Kai S. Exner[a,b,*], Lyuben Mihaylov[c], Diana Nihtianova[d], Kaloian Koynov[e], Konstantin Balashev[a]

[a] Department of Physical Chemistry, Faculty of Chemistry and Pharmacy, University of Sofia, 1 James Bourchier Blvd., 1164 Sofia, Bulgaria [b] Institute of Electrochemistry, Ulm University, Albert-Einstein-Allee 47, 89069 Ulm, Germany [c] Department of Applied Inorganic Chemistry, Faculty of Chemistry and Pharmacy, University of Sofia, 1 James Bourchier Blvd., 1164 Sofia, Bulgaria [d] Institute of Mineralogy and Crystallography, Bulgarian Academy of Sciences, Acad. G. Bonchev Str., bl. 107, 1113 Sofia, Bulgaria [e] Max Planck Institute for Polymer Research, D-55128 Mainz, Germany

ABSTRACT

Keywords:
Gold nanoparticles
Chitosan
UV–vis spectroscopy
Atomic force microscopy
Transmission electron microscopy
Apparent activation energy

In this work colloidal gold nanoparticles (GNPs) are prepared using a citrate-reduction route, in which citric acid serves as reductive agent for the gold precursor $HAuCl_4$. We demonstrate that a temperature variation on the one hand enables to tune the reaction rate of GNP formation and on the other hand allows modifying the morphology of the resulting metal nanoparticles. The use of chitosan, a biocompatible and biodegradable polymer with a multitude of functional amino and hydroxyl groups, facilitates the simultaneous synthesis and surface modification of GNPs in one pot. The resulting GNPs, which are stabilized by a network of chitosan and ß-ketoglutaric acid units, are characterized by UV–vis spectroscopy, atomic force microscopy (AFM), transmission electron microscopy (TEM) as well as fluorescence correlation spectroscopy (FCS) and reveal an average diameter of about 10 nm at the end of the synthesis. The kinetics of GNP formation is studied by calculating

1. Introduction

Due to their unique physical and chemical properties gold nanoparticles (GNPs) have attracted considerable scientific interest in several fields of chemistry, physics, material science, medicine or photonics since the second half of the 20th century [1–6]. In the literature various synthesis methods for producing GNPs are reported, such as micro emulsions, reversed micelles, seeding growth, sono-chemistry, photochemistry, radiolysis or direct chemical reduction [7–9]. From all these methods, the most efficient approach according to its simplicity constitutes the method of direct chemical reduction, in which goldcontaining precursors are reduced by a reducing agent [10]. The majority of synthesis protocols for the production of GNPs rely on a reduction of Au(III), e.g. $HAuCl_4$ or $AuCl_4^-$, to gold with oxidation state zero when a suitable reductant, commonly citrate [11] or borohydride [12] is added or generated in situ, e.g. by radiolysis of appropriate oligomers [13,14] into the reaction mixture. The so-called citrate synthesis, in which citrate serves as reductant, was introduced by Turkevich et al. [11] and later reinvestigated by Frens [15].

One of the key issues in colloid synthesis displays avoiding the aggregation of GNPs in order to obtain a monodisperse solution. In fact, sodium citrate in Turkevich′s synthesis [11] is playing an important role as stabilizing agent, which prevents aggregation and precipitation of the GNPs that reveal a compelling tendency to flocculate as a result of van der Waals interactions. Consequently, GNPs are successfully stabilized if an appropriate support or anions or polymers are available, which are shielding the surface of each nanoparticle [16]. The use of polymers in nanoparticle encapsulation for their further release by means of a semi-crystalline polymer matrix, which allows a better dispersion of the synthesized material, is one of the most promising techniques for the stabilization of nanoparticles′ dispersions [17,18].

Biosynthesis and green synthesis are other significant areas in GNPs preparation via in situ synthesis, in which the biomolecule may act as stabilizer and reductant both. Suitable sources for bio- and green preparations of GNPs are natural source extracts, for instance chitosan and microbes. Polysaccharides may also serve as stabilizing agents [19] according to their ability to coordinate metal ions. The resulting polymer-metal ion complex can then be reduced under mild conditions, yielding particles with smaller size and narrower size distribution in comparison to those synthesized in the absence of polymers, since the polysaccharide chains prevent the aggregation of the nanoparticles formed. Chitosan [20], starch [21], gum arabic [22] and alginate [23] are some examples of polysaccharides that were reported as stabilizing agents for the synthesis of metal nanoparticles. Chitosan constitutes a biocompatible, biodegradable, mucoadhesive, pH-dependent cationic polymer, which is insoluble in water at alkaline and neutral pH, and displays the second most abundant biopolymer in nature after cellulose. It consists of β–1,4 linked glucosamine and N-glucosamine units and can be synthesized by deacetylation of chitin. In acidic media chitosan′s amine groups become protonated ($R–NH_3^+$) so that the polymer is positively charged, which enables to solvate it in water. Furthermore, the ionic repulsion between the charged amine groups causes an extended linear polymer configuration. As polyelectrolyte chitosan is able to form electrostatic complexes under acidic conditions [24]. In presence of primary amino, hydroxyl or ester groups, chitosan is reconciled as excellent support material for metal nanoparticles by building networks with the above-mentioned functionalities that may protect the nanoparticle surface from aggregation. Chitosan stabilization of GNPs by adding $NaBH_4$ as reductant was first published in 2003 [25], while Huang et al. proposed a complete green synthesis of GNPs in 2004 claiming that chitosan acts both as reductive and stabilizing agent [26]. From this time onwards, chitosan-stabilized GNPs have found various applications in catalysis [27], biomedicine [28] and sensing [29].

In this article we report for a new synthesis of GNPs in presence of chitosan dissolved in citric acid, which enables the simultaneous synthesis and surface modification of GNPs in one pot. While so far in the literature either synthesis protocols for the formation of GNPs in presence of chitosan and acetic acid or in the presence of citric acid but in the absence of chitosan can be found, we demonstrate in this communication that the combination of citric acid and chitosan reveals major consequences in the size and shape of the produced GNPs as well as in the ongoing reaction mechanism as discussed in Section 3. We study the reaction kinetics of GNP formation by applying the FinkeWatzky model [30] and harmonic transition state theory in order to gains insights into activation parameters such as the apparent activation energy, entropy and free energy. The synthesized GNPs are characterized by different methods (cf. Section 2), such as ultraviolet-visible spectroscopy ((UV–vis)), atomic force microscopy (AFM), transmission electron microscopy (TEM) and fluorescence correlation spectroscopy (FCS).

2. Materials and methods

2.1. Chemicals and reagents

Analytical grade tetrachloroauric acid ($HAuCl_4 \cdot 3H_2O$) and trisodium citrate ($Na_3C_3H_5O(COO)_3 \cdot 2H_2O$) were obtained from Panreac Química S.A.U. (Spain) and Merck (Germany), respectively, while medium-molecular-weight chitosan, composed of β-(1–4)-linked D-glucosamine and N-acetyl-D-glucosamine with a deacetylation degree of about 75–85%, as well as citric acid (CA; $C_6H_8O_7$) were purchased from Sigma–Aldrich®. All solutions were prepared with deionized water.

2.2. Synthesis procedure

In our synthesis protocol, 1.0 wt. % of chitosan was dissolved in an aqueous solution of CA (1.0 wt. %) by stirring and heating the system at 50 °C for 24 h. Besides, a second solution was prepared, in which 10 mL of a 2.5 mM solution of tetrachloroauric acid ($HAuCl_4$) was added to 85 mL deionized water. The second mixture was stirred at 350 rpm and heated up to various temperatures, namely 50 °C, 60 °C, 70 °C, 80 °C and 90 °C. After that 5 mL of the first solution containing chitosan and CA was added to the solution of tetrachloroauric acid. During the synthesis of the GNPs the color of the solution changed from pink to red-violet.

2.3. Experimental methods

The obtained GNPs according to the above-presented synthesis procedure were characterized by ultraviolet–visible spectroscopy ((UV–vis)), atomic force microscopy (AFM), transmission electron microscopy (TEM) and fluorescence correlation spectroscopy (FCS).

2.3.1. Ultraviolet-visible spectroscopy ((UV–vis))

(UV–vis) absorption spectra of GNP dispersions were recorded by a spectrophotometer (Thermo Scientific Evolution 300, USA) at different reaction time intervals. Deionized water was used as reference sample.

2.3.2. Atomic force microscopy (AFM)

AFM imaging was performed on the NanoScope V system (Bruker Ltd, Germany) operating in tapping mode in air at room temperature.

We used silicon cantilevers (Tap 300Al-G, Budget Sensors, Innovative solutions Ltd, Bulgaria) with 30 nm thick aluminum reflex coatings. According to the producer's datasheet the cantilever spring constant and the resonance frequency are in the range of 1.5–15 N/m and 150 ± 75 kHz, respectively. The tip radius was less than 10 nm. The scan rate was set at 1 Hz and the images were captured in height mode with 512 × 512 pixels in JEPG format. Subsequently, all images were flattened by using NanoScope software. The same software was also used for section analysis and particle size determination.

The sample preparation for AFM imaging involved a deposition of the nanoparticle solution on a freshly cleaved mica surface by means of spin coating. Therefore, freshly cleaved quadratic mica sheets (Structure Probe Inc./SPI Supplies, West Chester, PA, USA) with a size of
10 × 10 mm glued to the metal pads were applied. An amount of about 100 μL of nanoparticle solution was deposited on the mica support. The corresponding samples of the nanoparticle solution were taken at different reaction times in accordance with the UV–vis measurements. For spin coating we applied Precision Spin Coater Model KW-4A (West Chester, PA, USA). Timer I was adjusted for 10 s. at 0.4 RPM and timer II for 60 s. at 2000 RPM. After spin coating the samples were thoroughly dried out with nitrogen gas and then transferred for AFM imaging.

2.3.3. Transmission electron microscopy (TEM)

The morphology and the size of the prepared GNPs were determined by JEOL-JEM-2100 LaB6 Transmission Electron Microscope (JEOL Ltd., Japan). The samples for TEM analysis were prepared by placing drops of GNP dispersions on carbon-coated TEM copper grids. After evaporation of the liquid the samples were analyzed. Size and size distribution were calculated statistically from TEM images.

2.3.4. Fluorescence correlation spectroscopy (FCS)

FCS experiments were performed using a commercial setup (Zeiss, Germany) consisting of the module ConfoCor 2 and an inverted microscope model Axiovert 200 with a Zeiss C-Apochromat 40 × /1.2 W water immersion objective. While an argon laser with wavelength of 488 nm was used for excitation, collected emission was filtered through a LP505 long pass filter before reaching the detector that consists of an avalanche photodiode in order to allow for single-photon counting. Eight-well polystyrene-chambered cover glass (Laboratory-Tek, Nalge Nunc International) was used as sample cell for the studied GNP dispersions. The confocal observation volume was calibrated using a reference dye with a known diffusion coefficient, namely Alexa Fluor 488.

3. Results and discussions

3.1. State of the art – literature survey

In the literature various schemes for the synthesis of GNPs in presence of chitosan can be found [31–35]. Most frequently, chitosan is dissolved in acetic acid. In all the above-mentioned studies, chitosan is identified as stabilizing agent for the obtained GNPs, while in some of these studies chitosan also serves as reductant. Since investigations of GNP formation in an aqueous solution of chitosan and citric acid (CA) have not been carried out yet, the literature does not reveal any mechanistic clues of GNP formation under the chosen experimental conditions (cf. Section 2.2). In Turkevich's citrate synthesis, CA constitutes the reductant for tetrachloroauric acid, thereby forming ß-ketoglutaric acid and a multitude of GNPs that are varying in their size and shape [11]. However, in an aqueous solution of chitosan and CA, either chitosan or CA may act as reductive agent for tetrachloroauric acid. Therefore, we are discussing the reaction mechanism of GNP formation for the chosen experimental parameters (cf. Section 2.2) in the following subsection.

3.2. Reaction mechanism of GNP formation in presence of chitosan and citric acid

In the first step of the synthesis, chitosan is dissolved in an aqueous CA solution (cf. Section 2.2). Chitosan reveals a multitude of functional amino and hydroxyl groups, while a hydroxyl group and carboxyl functionalities are prevalent in CA. In principle, three major interactions are conceivable: i) Interaction between the amino groups of chitosan and the carboxyl groups of CA resulting in the formation of amides; ii) Interaction between the hydroxyl groups of chitosan and the carboxyl groups of CA resulting in the formation of esters; iii) Electrostatic interactions between positively charged ammonium groups ($R–NH_3^+$) of chitosan and negatively charged carboxylate functions ($R–COO^-$) of CA. Amide formation can be clearly ruled out, since the interaction between an amino and a carboxyl group is kinetically hampered and requires temperatures higher than 100 °C. Quite in contrast, the reaction temperature of 50 °C may allow ester formation between hydroxyl groups of chitosan and carboxyl groups of CA, thereby producing an additional water molecule. However, ester formation constitutes an equilibrium reaction so that the yield is governed by the equilibrium constant. As water is the main component in the reaction mixture (98.0 wt. %), ester formation is strictly limited according to thermodynamics and thus can be neglected. Therefore, electrostatic interactions between positively charged ammonium and negatively charged carboxylate functions are reconciled as main interaction between chitosan and CA. This finding is also supported by the measured pH value of pH = 4.5, since an inspection of the corresponding pK_a values reveals that the amino groups ($R–NH_2$) of chitosan are protonated, thereby forming an ammonium group ($R–NH_3^+$), while the carboxyl functions of CA ((R–COOH)) are partially deprotonated, resulting in a carboxylate group (R–COO–). The electrostatic interactions between ammonium and carboxylate lead to the formation of an extended network of chitosan and CA molecules (cf. reaction Eq. (1) in Fig. 1).

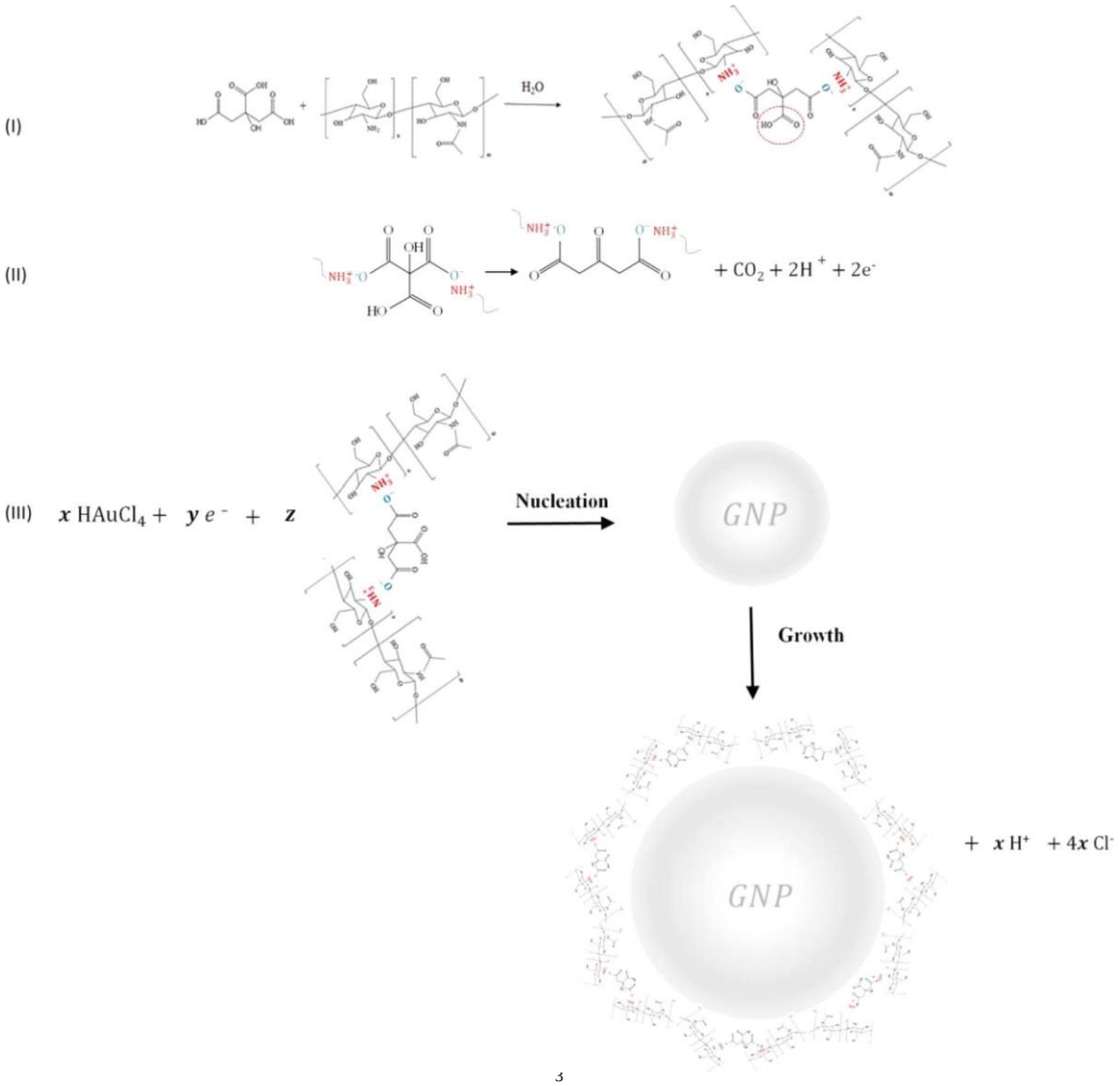

Fig. 1. Reaction mechanism for the formation of colloidal GNPs in an aqueous solution of CA and chitosan. In the first step, CA and chitosan form an extended network via electrostatic interactions between positively charged ammonium groups of chitosan and negatively charged carboxylate termini of CA. The addition of tetrachloroauric acid to this solution results in the oxidation of citrate, thereby producing ß-ketoglutaric acid under cleavage of CO_2 (step II). The released electrons are adopted by tetrachloroauric acid in order to reduce gold, thereby forming a GNP that is covered by a stabilizing protection shield consisting of chitosan units linked to ß-ketoglutaric acid (step III).

Such cross-linking of CA and chitosan has already been reported in literature previously [36].

In the second step of the synthesis, the aqueous solution of CA and chitosan is mixed with an aqueous solution of tetrachloroauric acid (cf. Section 2.2) giving rise to the occurrence of redox processes and GNP formation [37]. In the corresponding reduction reaction, Au(III) from tetrachloroauric acid is reduced to Au(0) in the bulk of the GNP, while gold atoms at the GNP surface might have some residual charge, e.g. Au (I). These reduction processes require the supply of electrons from a reductant, namely either CA or chitosan. In order to elucidate, whether CA or chitosan is serving as reductive agent, we need to consider all possible oxidative sites in both molecules. While in case of CA the hydroxyl group is oxidized to a ketone under cleavage of CO_2 and formation of ß-ketoglutaric acid [11], for chitosan as reductant either the hydroxyl groups may be oxidized to ketones (without cleavage of CO_2) or an amino functionality ($R–NH_2$) may be oxidized to a nitro group ($R–NO_2$). An oxidative decarboxylation of an alcohol to a ketone is energetically preferred over an oxidation of an alcohol to a ketone (without decarboxylation) according to the corresponding entropy gain (and thus free energy gain) by forming CO_2. Therefore, in case of chitosan oxidation, we only need to inspect the possible pathway for the oxidation of the amino functionality. For both competing pathways, namely oxidative decarboxylation of the hydroxyl group in case of CA and oxidation of the amino functionality for chitosan, we performed a thermodynamic analysis, in which formed and cleaved bonds of the initial and the final state were analyzed taking average bonding energies from thermodynamic data tables [38]. Entropy contributions are included in order to estimate the free energy of the corresponding oxidation reaction according to the Gibbs-Helmholtz equation:

$$\Delta G = \Delta H\, T- \cdot \Delta S \quad (1)$$

As average reaction temperature (cf. Section 2.2), T = 70 °C was chosen. Table 1 provides an overview of the competing oxidation processes.

Table 1 reveals that the free energy ΔG_{ox} for oxidative decarboxylation of CA is substantially smaller than for oxidation of the amino groups in chitosan. In case of CA the free energy of the reduction reaction, namely GNP formation, needs to fall below $\Delta G_{red} < -426$ kJ mol^{-1} in order to obtain an exergonic overall reaction, while oxidation of chitosan requires $\Delta G_{red} < -1874$ kJ mol^{-1}. Consequently, from a thermodynamic point of view CA is identified unambiguously as reductant for GNP formation. The thermodynamic analysis is also supported by kinetics: Since two electrons are transferred for the oxidative decarboxylation of CA, whereas six electrons are required for the sluggish amino group oxidation in chitosan, the kinetics of CA oxidation is assumed to proceed much faster than oxidation of chitosan according to a lower transition state free energy [41]. The detection of CA as reductant is additionally sustained by the fact that many of the amino (ammonium) groups in chitosan are forming an extended network with the carboxylate termini of CA or after oxidation of CA with ß-ketoglutaric acid (cf. reaction Eqs. (1) or (2) in Fig. 1), which prevents the amino groups to be available as reductant. Consequently, the influence of chitosan as possible reductive agent is negligible small and can be completely ruled out. Therefore, oxidative decarboxylation of CA under the formation of ß-ketoglutaric acid is identified as second step of the reaction mechanism (cf. reaction Eq. (2) in Fig. 1), which is followed by the reduction of Au(III) from tetrachloroauric acid (cf. reaction Eq. (3) in Fig. 1). The reduction of Au(III) under GNP formation according to reaction Eq. (3) consists of several elementary reaction steps [42–46]. In order to elucidate intermediate steps, in principle experimental techniques such as IR spectroscopy are required in order to identify possible reaction intermediates. In the further course we demonstrate (cf. Section 3.5) that our data can be ascribed to the model of Finke-Watzky [30] consisting of a homogeneous nucleation step that is followed by an autocatalytic surface growth. It is most likely that the formed GNPs reveal a protection shield consisting of chitosan linked with ß-ketoglutaric acid units, which may explain the high stability of the GNPs. The complete reaction mechanism is depicted in Fig. 1.

Table 1

Thermodynamic analysis of the competing oxidation processes for CA or chitosan oxidation. The change in energy (ΔH_{ox}) is determined by evaluating bonding energies from thermodynamic data tables [38], while the change in entropy (ΔS_{ox}) is obtained by taking only the standard entropies of CO_2 and H_2O into account assuming that the entropy change between the organic molecules is negligible small [39,40]. The free energy (ΔG_{ox}) of the corresponding oxidation process is calculated according to Eq. (1) for an average reaction temperature of T = 70 °C.

	CA	Chitosan
Oxidation reaction	R,R′-CHOH-CO_2H → R,R′-CO + CO_2 + 2H$^+$ + 2e$^-$	R-NH_2 + 2 H_2O → R-NO_2 + 6H$^+$ + 6e$^-$
ΔH_{ox}/kJ mol^{-1}	+500	+1826
ΔS_{ox}/J mol^{-1} K^{-1}	+214	−140
ΔG_{ox}/kJ mol^{-1}	+426	+1874

The presented reaction mechanism reveals the differences in size and shape of the obtained GNPs compared to Turkevich [11], whose GNPs suffer from a variety of different shapes (flat triangles, hexagons and bipyramidal forms) and sizes. All formed GNPs in presence of CA and chitosan show a spherical shape and a typical size distribution (cf. Section 3.4), which points out that the addition of chitosan into the solution may protect the surface of the GNPs, giving rise to the abovediscussed reaction mechanism, in which chitosan units in conjunction with ß-ketoglutaric acid are serving as stabilizing agent. The color of the solution that switches from colorless to violet, pink and red (cf. Fig. 2A) indicates the formation of stabilized colloidal GNPs, which further supports the chitosan linked to ß-ketoglutaric acid network on the GNP surface.

3.3. Absorption spectra of the GNPs according to UV–vis measurements

(UV–vis) absorption spectra of the GNPs′ dispersions were measured in the course of GNP formation taking the samples from the reaction mixture at certain times during the synthesis (cf. Section 2.3.1). The corresponding UV–vis spectrum as function of the reaction time for T = 70 °C is shown in Fig. 2.

The UV–vis spectrum in Fig. 2B exhibits the characteristic surface plasmon band of GNPs at a wavelength of about λ = 500–530 nm that can be firstly recognized after 5 min (Line 3) and which becomes more pronounced in the course of the synthesis. As the position and intensity of the absorption band is sensitive to size and shape of the GNPs, the increasing intensity of the absorption maximum in the course of the reaction corresponds to nanoparticle growth [47,48]. This finding may allow dividing the GNP formation into two separate parts, namely nucleation and growth, which is discussed in the further course of the manuscript (cf. Section 3.5).

The absorption maximum at λ = 530 nm in Fig. 2B corresponds to a red shift compared to Turkevich's GNPs formed by the according citrate route [11]. This red shift may be explained by the corresponding shell of chitosan and ß-ketoglutaric acid units (cf. Section 3.2) surrounding the GNP surface, which is not present in Turkevich's investigations according to the absence of chitosan.

3.4. Morphology of the GNPs according to AFM, TEM and FCS measurements

The morphology and the size of the synthesized GNPs were determined by means of AFM, TEM and FCS. AFM and TEM images of the formed GNPs are depicted in Fig. 3.

In Fig. 3C and D TEM images of the GNPs at the end of the synthesis are shown, which indicate that the synthesized GNPs are quite monodisperse. The particles reveal a spherical form with an average diameter of (11 ± 2) nm. The size of the GNPs at the end of the synthesis was confirmed also by AFM measurements, which are presented in Fig. 3A. The size of the GNP is confirmed by cross section analysis (cf. Fig. 3B) that indicates an average diameter of about 10 nm at the end of the synthesis.

The size of the obtained GNPs in an aqueous solution was estimated by fluorescence correlation spectroscopy [49–52]. The hydrodynamic diameter of

the GNPs determined by applying the corresponding model function of Ref. [43] amounts to (14 ± 5) nm. The relatively large error bars of the hydrodynamic diameter may be explained by a noisy autocorrelation curve as result of a weak luminescence signal. The difference in hydrodynamic diameter compared to the diameter of the dry samples in AFM and TEM studies may be ascribed to the stabilizing chitosan ß-ketoglutaric acid network on top of the GNP surface in conjunction with the aqueous surrounding, thus providing a larger diameter compared to AFM and TEM.

3.5. Kinetic analysis of the UV–vis and AFM data

From the UV−vis absorption spectrum in Fig. 2B the absorption maxima at λ = 530 nm as function of time t are taken and normalized with respect to the absorption of the maxima at the end of the synthesis (t = 50 min). This procedure is done for all five reaction temperatures, namely 50 °C, 60 °C, 70 °C, 80 °C and 90 °C (cf. Section 2.2). In Fig. 4 the normalized absorption maxima as function of the reaction time are plotted. The kinetic curves reveal a sigmoidal shape, which implies that the process of GNPs formation has an autocatalytic character and can be described by the Finke-Watzky model conveniently [30,53].

The Finke-Watzky model consists of two subsequent steps: First a slow, continuous and homogeneous nucleation process resulting in the formation of gold nuclei (rate constant k_1) that is followed by an autocatalytic surface growth of the GNPs (rate constant k_2). For a large excess of the reducing agent, i.e. CA, the corresponding system of differential equations can be solved according to Eq. (2) [53]:

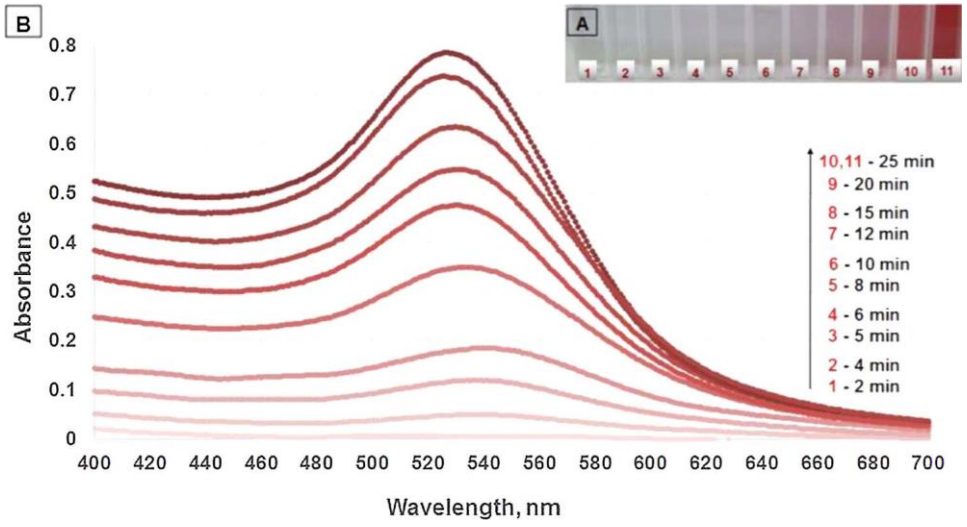

Fig. 2. (A)Photographic images of the samples at different times (between 2 min and 25 min, cf. right column) during the synthesis. (B) UV−vis absorption spectra for GNP formation in presence of chitosan and CA as function of the reaction time for T = 70 °C. The absorption maximum at 530 nm increases significantly during the synthesis.

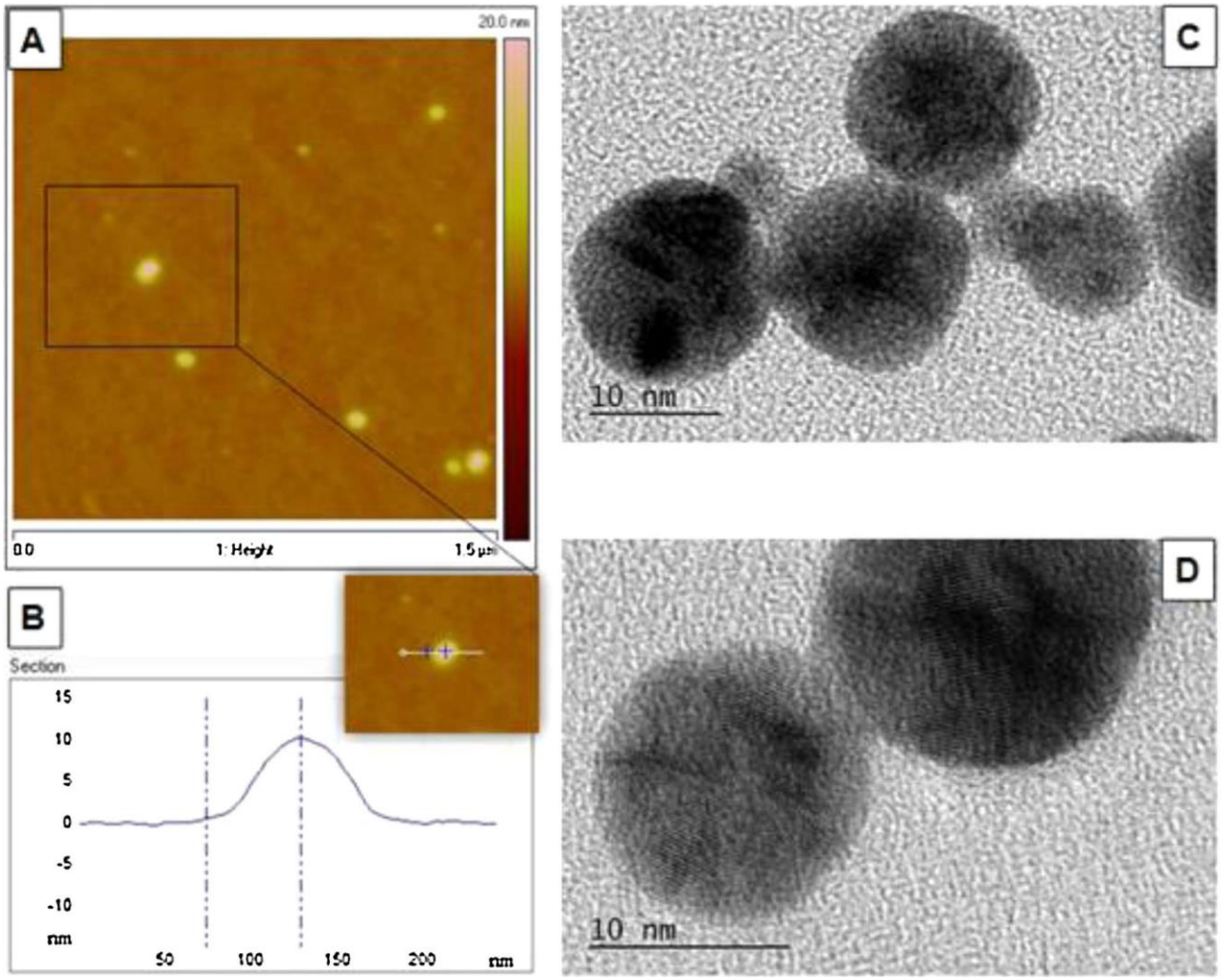

Fig. 3. (A) 2D AFM images and (B) cross section of the individual particle. (C) and (D) TEM images with magnification 10 nm.

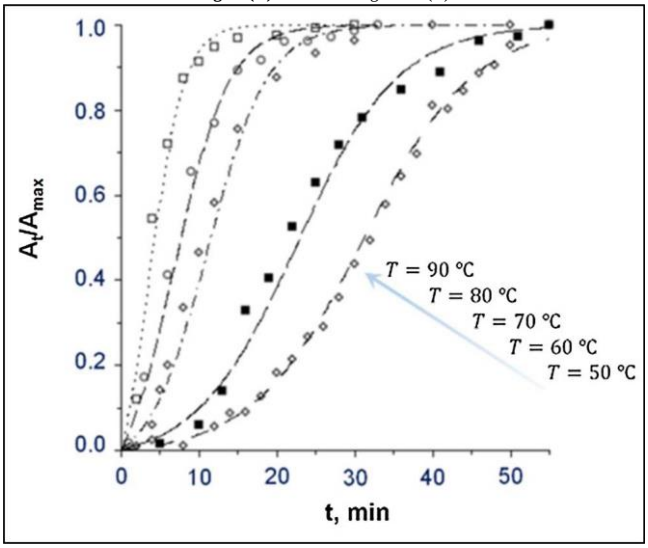

Fig. 4. Normalized absorption maxima at λ = 530 nm as function of time t for different reaction temperatures (50 °C, 60 °C, 70 °C, 80 °C and 90 °C). The sigmoidal shape of the curves indicates that the model of Finke and Watzky [29] can be applied, which facilitates to divide the GNP formation into two parts, namely nucleation and growth.

$$[A]_t = \frac{\frac{k_1}{k_2} + [A]_0}{1 + \frac{k_1}{k_2[A]_0} e^{(k_1 + k_2[A]_0)t}} \quad (2)$$

In Eq. (2) k_1 and k_2 denote the rate constants for the processes of nucleation and growth, respectively, while $[A]_t$ and $[A]_0$ indicate the concentration of tetrachloroauric acid as function of reaction time and the concentration of tetrachloroauric acid at the beginning of the synthesis, respectively.

For analyzing the GNPs growth the extinction cross section C_{ext} is calculatd, which depends on the nanoparticle diameter d, the wavelength λ, the dielectric constant of the medium (water) $\varepsilon_m = 1.775$ as well as of the dielectric function of the GNPs that consists of a real part ε_{Re} and a imaginary part ε_{Im}:

$$C_{ext} = \frac{3\pi^2 d^3 \varepsilon_m^{3/2}}{\lambda} \frac{\varepsilon_{Im}}{(\varepsilon_{Re} + 2\varepsilon_m)^2 + \varepsilon_{Im}^2} \quad (3)$$

Comparing the extinction cross section C_{ext} with the experimentally measured absorbance A reveals that both quantities are proportional by a factor of 3.05×10^{15}. This value differs only by about 10% compared to the idealized case of a monodisperse solution of GNPs with a spherical shape for which 2.70×10^{15} was obtained as proportional constant [53]. For λ = 520 nm, the real part of the dielectric function ε_{Re} matches $-2\,\varepsilon_m$ so that Eq. (3) can be simplified to:

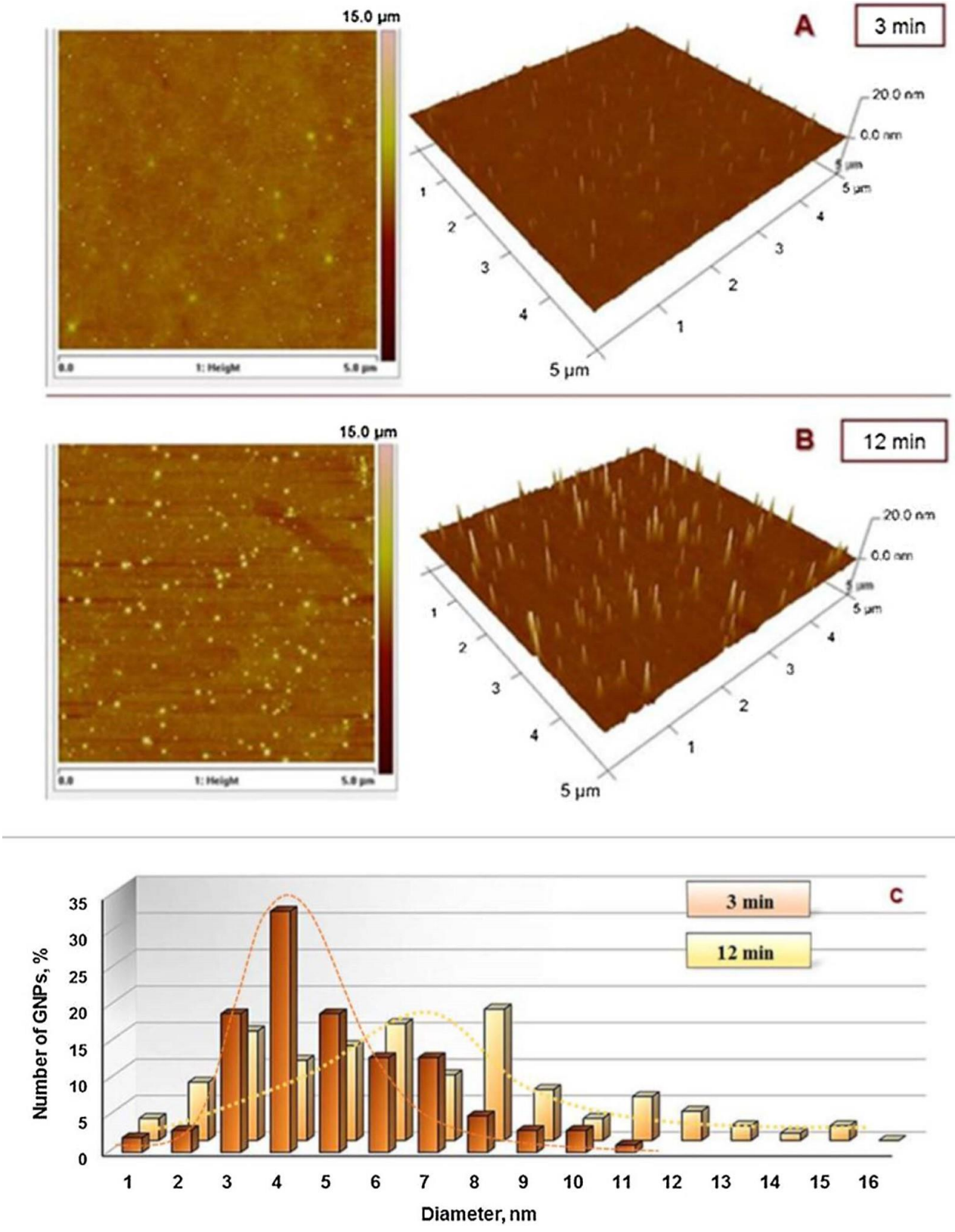

Fig. 5. AFM 2D and 3D images obtained during the synthesis after 3 min (A) and after 12 min (B) for T = 70 °C. Histogram of GNP size distribution after 3 min and 12 min according to the corresponding AFM images (C).

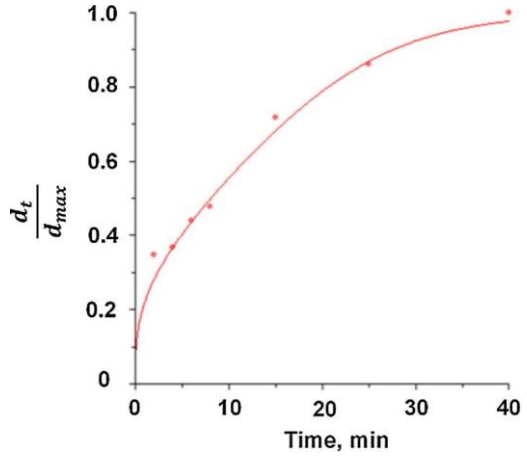

Fig. 6. Normalized GNP diameter (based on the maximum of the size distribution) as function of the reaction time according to the model of Finke and Watzky (cf. Eq. (6)). The optimized fit function (solid red line) facilitates to calculate the rate constants for nucleation (k_1) and growth (k_2).

Table 2

Rate constants for nucleation (k_1) and growth (k_2) according to the Finke-Watzky model obtained from UV–vis and AFM measurements as function of the reaction temperature. AFM measurements were performed only for T = 70 °C.

Synthesis Temperature	UV–vis Measurements		AFM Measurements	
	k_1/s^{-1}	$k_2/M^{-1}s^{-1}$	k_1/s^{-1}	$k_2/M^{-1}s^{-1}$
50 °C	1.7×10^{-3}	0.14	–	–
60 °C	4.5×10^{-3}	0.15	–	–
70 °C	1.3×10^{-2}	0.25	$1.1 \cdot 10^{-2}$	0.22
80 °C	3.0×10^{-2}	0.27	–	–
90 °C	7.0×10^{-2}	0.39	–	–

$$C_{ext} = \frac{3\pi^2 \varepsilon_m^{3/2}}{\lambda} \frac{1}{\varepsilon_{Im}} d^3 \sim A \quad (4)$$

Since for GNPs up to a size of 20 nm the function ε_{Im} is constant [27], the extinction cross section C_{ext} depends on the nanoparticle diameter only, since the term can be summarized as constant K:

$$C_{ext} = K \cdot d^3 \sim A \Longrightarrow C_{ext}^{1/3} \sim A^{1/3} \sim d \quad (5)$$

Eq. (5) enables to connect the experimentally measured kinetic data from the UV–vis measurements with other experimental methods such as AFM in order to gain insights into the GNP size in the course of the synthesis. Combining Eqs. (2) and (5) by considering the law of Lambert-Beer results in [53]:

$$\frac{d_t}{d_{max}} = \left(1 - \frac{k_1 + k_2[\mathrm{A}]_0}{k_2[\mathrm{A}]_0 + k_1 e^{(k_1 + k_2[\mathrm{A}]_0)t}}\right)^{\frac{1}{3}} \quad (6)$$

In Eq. (6) d_t and d_{max} denote the diameter of the GNP at any time during the synthesis and at the end of the synthesis, respectively. In Fig. 5A and B, AFM images corresponding to spin-coated samples of the reaction solution at t = 3 min and t = 12 min are shown for T = 70 °C. After 3 min, the average diameter of the GNPs amount to (4.2 ± 0.5) nm according to cross section analysis, while after 12 min the GNP diameter has grown to (6.5 ± 1.5) nm. The corresponding size distribution for both reaction times from an analysis of about 300 nanoparticles is presented in Fig. 5C, which indicates that the maximum of the distribution shifts from 4 nm to a diameter of 8 nm for t = 3 min and t = 12 min, respectively.

The same analysis as presented in Fig. 5 was done for all measured reaction times in order to determine the maximum of the size distribution (d_t) as function of time that is normalized by taking the size distribution maximum as the end of the synthesis (d_{max}). The normalized size distribution maximum as function of time is plotted according to Eq. (6) in Fig. 6. It turns out that the calculated fit function according to the Finke-Watzky model [30,53] describes the processes of nucleation and growth reasonably well.

Based on the obtained fit function (solid red line in Fig. 6) kinetic parameters, namely the rate constants for nucleation (k_1) and growth (k_2) can be estimated corresponding to to Eq. (6). The same procedure was established with the corresponding UV–vis data (cf. Fig. 4). Table 2 summarizes the calculated rate constants.

Comparing the rate constants obtained from UV–vis and AFM investigations for a reaction temperature of T = 70 °C it turns out that the values differ by about 10%, which constitutes a reasonably good agreement.

The knowledge of the rate constants as function of the reaction temperature allows gaining insights into kinetic activation parameters for nucleation and growth based on an Arrhenius plot or an Arrhenius-like plot [54]. Using the relation

$$\ln k = \ln A - \frac{E_A}{R} \frac{1}{T} \quad (7)$$

enables to determine the activation energies (E_A) from the slope of the corresponding ln k vs. 1/T Arrhenius plot, while the pre-exponential factor A is accessible from the intercept of the ln k axis. In Eq. (7),
R = 8.314 J/(mol·K) denotes the universal gas constant.

Applying harmonic transition state theory according to the concept of Eyring, in which the pre-exponential factor is assumed to scale with temperature, enables to determine the apparent activation energy ($\Delta H^{\#}$) as well as the apparent activation entropy ($\Delta S^{\#}$) by the corresponding ln k/T vs. 1/T plot [54]:

$$\ln \frac{k}{T} = \ln \frac{k_B}{h} + \frac{\Delta S^{\#}}{R} - \frac{\Delta H^{\#}}{R} \frac{1}{T} \quad (8)$$

In Eq. (8) $k_B = 1.38 \cdot 10^{-23}$ J/K and $h = 6.626 \cdot 10^{-34}$ J·s denote Boltzmann's and Planck's constant, respectively. In Fig. 7A and B the corresponding plots according to Eq. (7) and Eq. (8), respectively are presented. The calculated kinetic activation parameters for nucleation and growth are summarized in Table 3.

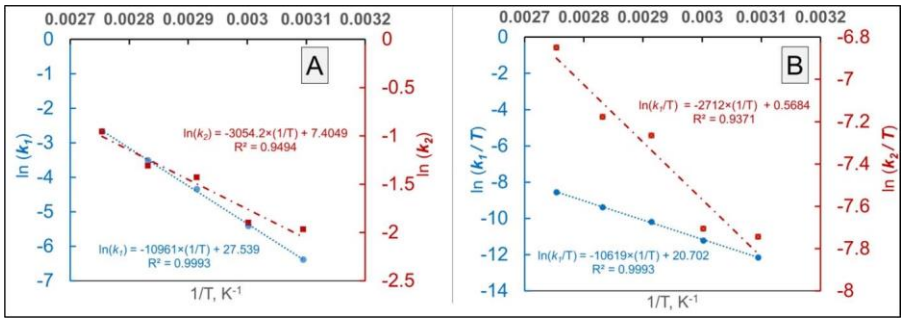

Fig. 7. (A) Arrhenius plot according to Eq. (7) in order to obtain the pre-exponential factor A and the activation energy E_A for both processes, namely nucleation and growth. (B) Arrhenius-like plot according to Eq. (8) that enables determining the apparent activation energy and the apparent activation entropy.

Table 3

Kinetic activation parameters, namely pre-exponential factor A, activation energy E_A, apparent activation energy $\Delta H^{\#}$ and apparent activation entropy $\Delta S^{\#}$ for nucleation and growth corresponding to the plots in Fig. 7A and B. The apparent free activation energy $\Delta G^{\#}$ is calculated for an average reaction temperature of T = 70 °C according to Eq. (1).

Process	A/L mol^{-1} s^{-1}	E_A/kJ mol^{-1}	$\Delta H^{\#}$/kJ mol^{-1}	$\Delta S^{\#}$/J/mol K	$\Delta G^{\#}$/kJ mol^{-1}
Nucleation	1.61×10^{12}	92.7	89.8	−19.2	96.4
Growth	1.24×10^{3}	24.6	21.7	−194	88.3

Table 3 indicates that the activation energy E_A and the apparent activation energy $\Delta H^{\#}$ for the processes of nucleation and growth almost match each other. Comparing the subsequent processes of nucleation and growth it turns out that the pre-exponential factor for nucleation is nine orders of magnitude larger than that for growth, whereas the activation energy and the apparent activation energy for growth are significantly smaller by almost 70 kJ/mol. Quite in contrast, growth suffers from a considerable decrease in the apparent activation entropy, whereas the entropy change for nucleation is almost negligible small. Applying the Gibbs-Helmholtz relation of Eq. (1) enables to calculate the apparent free activation energy $\Delta G^{\#}$ for nucleation as well as for growth. It turns out that $\Delta G^{\#}$ for growth is by about 8 kJ/mol smaller compared to nucleation for an average reaction temperature of T = 70 °C.

Interestingly, the processes of nucleation and growth reveal completely different characteristic concerning its activation parameters: While for nucleation the apparent free activation energy $\Delta G^{\#}$ is governed by the apparent activation energy $\Delta H^{\#}$, since the $-T \cdot \Delta S^{\#}$ term contributes less than 7% to $\Delta G^{\#}$, the entropy contribution ($-T \cdot \Delta S^{\#}$) exceeds the apparent activation energy $\Delta H^{\#}$ by a factor of 3 for growth. The significant decrease in entropy for growth can be interpreted in terms of the Arrhenius Eq. (7) that according to the complexity of the reactant molecule the steric factor of the growing Au cluster is extremely small resulting in the dwarfish pre-exponential factor for growth. Calculating the ratio of the rate constants for growth and nucleation by taking the apparent free activation energy $\Delta G^{\#}$ for T = 70 °C (cf. Table 3), it turns out that the process of GNP growth is by a factor of 17 faster than nucleation. This finding may be a starting point of further investigations in the future to understand why the apparent free activation energy $\Delta G^{\#}$ is ruled by the apparent activation entropy for a fast process (growth), while for a slow process (nucleation) the apparent activation energy is substantially prevailing over the apparent activation entropy. For this purpose ab initio methods such as density functional theory (DFT) calculations are called for, e.g. the determination of the free energy landscape along the reaction coordinate in conjunction with microkinetic modeling [55] may allow deeper conclusions concerning the apparent activation energy and the apparent free activation energy, while molecular dynamics (MD) simulations may be helpful for a deeper understanding of entropy contributions.

4. Conclusions

In this article we propose a new synthesis of GNPs in presence of CA and chitosan with tetrachloroauric acid as precursor based on a citrate reduction route. The discussion of the reaction mechanism (cf. Section 3.2) reveals that CA is identified as reductant, while a network of chitosan and ß-ketoglutaric acid units on the GNP surface is reconciled as stabilizing agent, hence explaining the high stability of the nanoparticles formed. The synthesized GNPs are characterized by various methods such as UV−vis (cf. Section 3.3), AFM, TEM and FCS (cf. Section 3.4). The kinetics of GNP formation is studied by UV−vis and AFM data applying the Finke-Watzky model [30,53] and harmonic transition state theory in order to calculate activation parameters such as the apparent activation energy, entropy and free energy for nucleation and growth (cf. Section 3.5). Further ab initio based studies are called for in order to gain in-depths insights into the elementary reaction steps during GNP formation, which allow a profound interpretation of the experimentally based kinetic data by combining experiment and theory [56,57].

Acknowledgements

All authors are grateful for financial support within the Horizon 2020 Materials Networking Project (H2020-TWINN-2015-Twinning). SS, PG and LM are grateful to the operational program "Science and Education for Smart Growth", project BG05M2OP001-2.009-0028, while KSE acknowledges funding from the Alexander von Humboldt Foundation.

References

[1] M.C. Daniel, D. Astruc, Gold nanoparticles: assembly, supramolecular chemistry, quantum-size-related properties, and applications toward biology, catalysis, and nanotechnology, Chem. Rev. 104 (2004) 293–346.

[2] S.J. Guo, E.K. Wang, Synthesis and electrochemical applications of gold nanoparticles, Anal. Chim. Acta 598 (2007) 181–192.

[3] E. Boisselier, D. Astruc, Gold nanoparticles in nanomedicine: preparations, imaging, diagnostics, therapies and toxicity, Chem. Soc. Rev. 38 (2009) 1759–1782.

[4] S.H. Radwan, H.M. Azzazy, Gold nanoparticles for molecular diagnostics, Expert Rev. Mol. Diagn. 9 (2009) 511–524.

[5] W.R. Algar, M. Massey, U.J. Krull, The application of quantum dots, gold nanoparticles and molecular switches to optical nucleic-acid diagnostics, Trends Anal. Chem. 28 (2009) 292–306.

[6] W.E. Bawarski, E. Chidlowsky, D.J. Bharali, S.A. Mousa, Emerging nanopharmaceuticals, Nanomed. Nanotechnol. 4 (2008) 273–282.

[7] C. Roos, M. Schmidt, J. Ebenhoch, F. Baumann, B. Deubzer, J. Weis, Design and synthesis of molecular reactors for the preparation of topologically trapped gold clusters, Adv. Mater. 11 (1999) 761–766.

[8] R.G. Freeman, M.B. Hommer, K.C. Grabar, M.A. Jackson, M.J. Natan, Ag-clad Au nanoparticles: novel aggregation, optical, and surface-enhanced Raman scattering properties, J. Phys. Chem. 100 (1996) 718–724.

[9] L. Cao, P. Diao, L. Tong, T. Zhu, Z. Liu, Surface-enhanced Raman scattering of paminothiophenol on a Au (core)/Cu (shell) nanoparticle assembly, Chem. Phys. Chem. 6 (2005) 913–918.

[10] N. Toshima, T. Yonezawa, Bimetallic nanoparticles - novel materials for chemical and physical applications, New J. Chem. 22 (1998) 1179–1201.

[11] J. Turkevich, P.C. Stevenson, J. Hillier, A study of the nucleation and growth processes in the synthesis of colloidal gold, Discuss. Faraday Soc. 11 (1951) 55–75.

[12] P.C. Lee, D. Meisel, Adsorption and surface-enhanced Raman of dyes on silver and gold sols, J. Phys. Chem. 86 (1982) 3391–3395.

[13] M. Sakamoto, T. Tachikawa, M. Fujitsuka, T. Majima, Acceleration of laser-induced formation of gold nanoparticles in a poly(vinyl alcohol) film, Langmuir 22 (2006) 6361–6366.

[14] T.K. Sau, A. Pal, N.R. Jana, Z.L. Wang, T. Pal, Size controlled synthesis of gold nanoparticles using photochemically prepared seed particles, J. Nanopart. Res. 3 (2001) 257–261.

[15] J.G. Frens, Controlled nucleation for the regulation of the particle size in monodisperse gold suspensions, Nature 241 (1973) 20–22.

[16] P. Tartaj, T. Gonzalez-Carreño, C.J. Serna, Synthesis of nanomagnets dispersed in colloidal silica cages with applications in chemical separation, Langmuir 18 (2002) 4556–4558.

[17] A.I. Frenkel, C.W. Hills, R.G. Nuzzo, A view from the inside: complexity in the atomic scale ordering of supported metal nanoparticles, J. Phys. Chem. B 105 (2001) 12689–12703.

[18] K.J. Klabunde, J. Habdas, G. Cardenas-Triviño, Colloidal metal particles dispersed in monomeric and polymeric styrene and methyl methacrylate, Chem. Mater. 1 (1989) 481–483.

[19] Z. Gao, R. Su, R. Huang, W. Qi, Z. He, Glucomannan-mediated facile synthesis of gold nanoparticles for catalytic reduction of 4-nitrophenol, Nanoscale Res. Lett. 9 (2014) 404.

[20] D.K. Božanić, L.V. Trandafilović, A.S. Luyt, V. Djoković, 'Green' synthesis and optical properties of silver-chitosan complexes and nanocomposites, React. Funct. Polym. 70 (2010) 869–873.

[21] P. Raveendran, J. Fu, S.L. Wallen, A simple and green method for the synthesis of Au, Ag and Au-Ag alloy nanoparticles, Green Chem. 8 (2006) 34–38.

[22] P.S. Gils, D. Ray, P.K. Sahoo, Designing of silver nanoparticles in gum arabic based semi-IPN hydrogel, Int. J. Biol. Macromol. 46 (2010) 237–244.

[23] V. Jaouen, R. Brayner, D. Lantiat, N. Steunou, T. Coradin, In situ growth of gold colloids within alginate films, Nanotechnology 21 (2010) 185605.

[24] R. Marguerite, Chitin and chitosan: properties and application, Prog. Polym. Sci. 31 (2006) 603–632.

[25] K. Esumi, N. Takei, T. Yoshimura, Antioxidant-potentiality of gold-chitosan nanocomposites, Colloid. Surf. B 32 (2003) 117–123.

[26] H. Huang, X. Yang, Synthesis of chitosan-stabilized gold nanoparticles in the absence/presence of tripolyphosphate, Biomacromolecules 5 (2004) 2340–2346.

[27] A. Primo, F. Quignard, Chitosan as efficient porous support for dispersion of highly active gold nanoparticles: design of hybrid catalyst for carbon-carbon bond formation, Chem. Commun. 46 (2010) 5593–5595.

[28] L.C. Cheng, J.H. Huang, H.M. Chen, T.C. Lai, K.Y. Yang, R.S. Liu, M. Hsiao, C.H. Chen, L.J. Her, D.P. Tsai, Seedless, silver-induced synthesis of star-shaped gold/silver bimetallic nanoparticles as high efficiency photothermal therapy reagent, J. Mater. Chem. 22 (2012) 2244–2253.

[29] F. Porta, Z. Krpetic, L. Prati, A. Gaiassi, G. Scari, Gold-ligand interaction studies of water-soluble aminoalcohol capped gold nanoparticles by NMR, Langmuir 24 (2008) 7061–7064.

[30] M. Watzky, R. Finke, Transition metal nanocluster formation kinetic and mechanistic studies. A new mechanism when hydrogen is the reductant: slow continuous nucleation and fast autocatalytic surface growth, J. Am. Chem. Soc. 119 (1997) 10382–10400.

[31] M. Adlim, M.A. Bakar, Preparation of chitosan-gold nanoparticles: part 1. Effect of reducing technique, Indones. J. Chem. 8 (2008) 184–188.

[32] M. Adlim, M.A. Bakar, Preparation of chitosan-gold nanoparticles: part 2. The role of chitosan, J. Chem. 8 (2008) 320–326.

[33] N.D.K. Vo, E. Guillon, L. Dupont, C. Kowandy, X. Coqueret, Influence of Au (III) interactions with chitosan on gold nanoparticle formation, J. Phys. Chem. C 118 (2014) 4465–4474.

[34] C.-M. Shih, Y.-T. Shieh, Y.-K. Twu, Preparation of gold nanopowders and nanoparticles using chitosan suspensions, Carbohydr. Polym. 78 (2009) 309–315.

[35] N.M. Sultan, M.R. Johan, Synthesis and ultraviolet visible spectroscopy studies of chitosan capped gold nanoparticles and their reactions with analytes, Sci. World J. (2014) 184604–184610.

[36] J. Varshosaz, R. Alinagari, Effect of citric acid as cross-linking agent on insulin loaded chitosan microspheres, Iran. Polym. J. 14 (2005) 647–656.

[37] P. Raveendran, J. Fu, S.L. Wallen, A simple and "green" method for the synthesis of Au, Ag, and Au–Ag alloy nanoparticles, Green Chem. 8 (2005) 34–38.

[38] P.W. Atkins, J. de Paula, Physical chemistry, Fifth Completely Revised Edition, German edition, Wiley-VCH, 2006.

[39] K.S. Exner, J. Anton, T. Jacob, H. Over, Chlorine evolution reaction on RuO_2(110): Ab initio atomistic thermodynamics study – pourbaix diagrams, Electrochim. Acta 120 (2014) 460–466.

[40] K.S. Exner, J. Anton, T. Jacob, H. Over, Controlling selectivity in the chlorine evolution reaction over RuO_2-based catalysts, Angew. Chem. Int. Ed. 53 (2014) 11032–11035.

[41] K.S. Exner, H. Over, Kinetics of electrocatalytic reactions from first-principles: a critical comparison with the Ab initio thermodynamics approach, Acc. Chem. Res. 50 (2017) 1240–1247.

[42] X. Ji, X. Song, J. Li, Y. Bai, W. Yang, X. Peng, Size control of gold nanoparticles in citrate reduction: the third role of citrate, J. Am. Chem. Soc. 129 (2007) 13939–13948.

[43] D. Li, Q. He, Y. Cui, K. Wang, X. Zhang, J. Li, Thermosensitive copolymer networks modify gold nanoparticles for nanocomposite entrapment, Chem. Eur. J. 13 (2007) 2224–2229.

[44] D. Li, Y. Chi, K. Wang, Q. He, X. Yan, J. Li, Thermosensitive nanostructures comprising gold nanoparticles grafted with block copolymers, Adv. Funct. Mater. 17 (2007) 3134–3140.

[45] D. Li, Q. He, J. Li, Smart core/shell nanocomposites: intelligent polymers modified gold nanoparticles, Adv. Colloid Interface Sci. 149 (2009) 28–38.

[46] N. Li, K. Wang, Y. Gao, D. Li, W. Lin, C. Li, Tartrate as a substitute of citrate to prepare gold colloids from chloroauric acid, Colloids Surf. A 535 (2017) 251–256. [47] L.M. Liz-Marzàn, Nanometals: formation and color, Mater. Today 7 (2004) 26–31.

[48] P. Mulvaney, Surface plazmon spectroscopy of nanosized metal particles, Langmuir 12 (1996) 788–800.

[49] K. Koynov, H.-J. Butt, Fluorescence correlation spectroscopy in colloid and interface science, Curr. Opin. Colloid Interface Sci. 17 (2012) 377–387.

[50] C.L. Kuyper, K.L. Budzinski, R.M. Lorenz, D.T. Chiu, Real-time sizing of nanoparticles in microfluidic channels using confocal correlation spectroscopy, J. Am. Chem. Soc. 128 (2006) 730–731.

[51] K. Wang, X. Qiu, C. Dong, J.C. Ren, Single-molecule technology for rapid detection of DNA hybridization based on resonance light scattering of gold nanoparticles, Chembiochem. 8 (2007) 1126–1129.

[52] A. Tcherniak, S. Dominguez-Medina, W.-S. Chang, P. Swanglap, L.S. Slaughter, C.F. Landes, One-photon plasmon luminescence and its application to correlation spectroscopy as a probe for rotational and translational dynamics of gold nanorods, J. Phys. Chem. C 115 (2011) 15938–15949.

[53] P. Georgiev, A. Bojinova, B. Kostova, D. Momekova, T. Bjornholm, K. Balashev, Implementing atomic force microscopy (AFM) for studying kinetics of gold nanoparticle's growth, Colloids Surf. A 434 (2013) 154–163.

[54] I. Sohrabnejad-Eskan, A. Goryachev, K.S. Exner, L.A. Kibler, E.J.M. Hensen, J.P. Hofmann, H. Over, Temperature-dependent kinetic study of the chlorine evolution reaction over RuO_2(110) model electrodes, ACS Catal. 7 (2017) 2403–2411.

[55] K.S. Exner, J. Anton, T. Jacob, H. Over, Full kinetics from first principles of the chlorine evolution reaction over a RuO_2(11) model electrode, Angew. Chem. Int. Ed. 55 (2016) 7501–7504.

[56] K.S. Exner, I. Sohrabnejad-Eskan, J. Anton, T. Jacob, H. Over, Full free energy diagram of an electrocatalytic reaction over a single-crystalline model electrode, ChemCatChem 4 (2017) 2902–2908.

[57] K.S. Exner, I. Sohrabnejad-Eskan, H. Over, A universal approach to determine the free energy diagram of an electrocatalytic reaction, ACS Catal. 8 (2018) 1864–1879.